Arch. Metall. Mater. **67** (2022), 4, 1333-1339

DOI: https://doi.org/10.24425/amm.2022.141059

BIN SU[1], JING-YUAN LIU[1], XIAO-PENG ZHANG[1], XUE-WEI YAN[2*]

SIMULATION OF DENDRITE MORPHOLOGY AND MICRO-SEGREGATION IN U-Nb ALLOY DURING SOLIDIFICATION

Due to the importance of uranium and uranium alloys to national defence and nuclear industrial applications, it is necessary to understand dendrite formation in their solidification structures and to control their microstructures. In this study, a modified cellular automaton model was developed to predict 2-D and 3-D equiaxed dendrite growth in U-Nb alloys. The model takes into account solute diffusion, preferential growth orientation, interface curvature, etc., and the solid fraction increment is calculated using the local level rule method. Using this model, 2-D large-scale and 3-D equiaxed dendrite growth with various crystallographic orientations in the U-5.5Nb alloy were simulated, and the Nb micro-segregation behaviour during solidification was analysed. The simulated results showed reasonable agreement with the as-cast microstructure observed experimentally.

Keywords: U-Nb alloys; solidification process; dendrite growth; cellular automaton; numerical simulation

1. Introduction

Uranium and its alloys are widely used in the national defence and nuclear energy engineering fields due to their high densities and unique nuclear properties [1-3]. For example, adding niobium to uranium is an effective way to improve its mechanical properties and corrosion resistance. As is well known, the microstructure of a material is the strategic link between processing and performance, and thus an understanding of microstructure solidification is necessary to improve material mechanical properties and to design heat treatment processes. U-Nb alloys have a large solidification temperature range and easily form micro-segregations after solidification because the diffusion of niobium in uranium is extremely slow [4]. Therefore, it is of great importance to investigate the formation and evolution of related solidification structures.

Experimental research on U-Nb alloys remains limited owing to the associated high costs and radioactive hazards. In recent years, modelling and simulations have been widely used as powerful tools to aid in the understanding of the fundamentals of dendrite morphology and micro-segregation during solidification. Various computational models such as cellular automaton (CA) [5-12], Monte Carlo [13], and phase field [14-16], have been developed to simulate microstructural evolution during the solidification process. Among these methods, the CA model is effective for revealing a wide scale range of microstructural features and has the advantages of a high calculation efficiency and clear physical meaning [10]. Therefore, it is widely used in the study of microstructural evolution in many different alloys. However, until now, little research has been done on microstructural simulations of U-Nb alloys because of the lack of experimental data. Moreover, although adaptive mesh refinement and parallel computing methods have been proposed to improve the computation efficiency, 3-D dendritic morphology and large-scale simulations remain a challenge.

In this work, a modified CA model was developed to simulate the formation and evolution of the primary phase in the U-5.5Nb alloy during the solidification process. Using the model, 2-D and 3-D equiaxed dendrite growth were simulated, and the evolution of Nb micro-segregation was investigated. Experiments were carried out, and the capability of the model to describe the microstructural evolution was discussed.

2. Model description

The CA method was used for the simulation. The computational domain is uniformly discretized into square cells for 2D simulations or cubic cells for 3D simulations. Each cell has several variables including temperature (T), solute content

[1] CHINA ACADEMY OF ENGINEERING PHYSICS, INSTITUTE OF MATERIALS, JIANGYOU, CHINA
[2] ZHENGZHOU UNIVERSITY OF AERONAUTICS, SCHOOL OF AERO ENGINE, ZHENGZHOU, CHINA
* Corresponding author: yanxuewei@zua.edu.cn

(C_S and C_L), solid fraction (f_S), and crystallographic orientation (θ). The cell is characterized by the solid ($f_S = 1$), liquid ($f_S = 0$), and S/L interface ($0 < f_S < 1$). At the beginning of the simulation, each cell is set as a liquid state with the same initial temperature and initial concentration. In this model, the dendrite growth process of the primary phase was simulated, including nucleation, growth, and coarsening of dendrite arms, as well as interactions between surrounding dendrites and the solute distribution behaviour. The simulation ends when the temperature decreases to a point just before occurrence of the binary monotectoid transformation. The governing equations used to calculate solid fraction, distribution of concentration, growth velocity of the S/L interface, and capturing rules are described in detail below.

2.1. Nucleation model

A continuous Gaussian nucleation distribution model [5] was employed in the nucleation process, and the density of nucleus $n(\Delta T)$ at a given undercooling ΔT is given as follows:

$$n\left(\Delta T\right) = \int_0^{\Delta T}\left[1 - f_{Solid}\left(\Delta T'\right)\right]\frac{dn}{d\left(\Delta T'\right)}d\left(\Delta T'\right) \tag{1}$$

$$\frac{dn\left(\Delta T\right)}{d\left(\Delta T'\right)} = \frac{N_{\max}}{\sqrt{2\pi}\Delta T_\sigma}\exp\left(-\frac{1}{2}\left(\frac{\Delta T' - \Delta T_N}{\Delta T_\sigma}\right)^2\right) \tag{2}$$

where ΔT is the undercooling, $n(\Delta T)$ is the nucleus density, $f_{Solid}(\Delta T')$ is the fraction of solid phase, $N_{\max}$ is the maximum nucleus density, ΔT_N is the mean nucleation undercooling, ΔT_σ is the standard deviation of the distribution, and $\Delta T'$ is the undercooling integral element. The primary phase dendrites is expected to nucleate when temperature falls below the liquidus [17]. The newly formed nuclei are randomly distributed in the domain, and the total grain density can be obtained at any undercooling ΔT according to Eq. (1) and Eq. (2). Once the cell is nucleated, the index of the cell is changed to "growing" associated with a random preferential growth direction θ [10]. The capture process for a cell begins only when the cell is selected as primary phase nucleus (or totally solidified), it will alter its surrounding liquid neighbors into S/L interface state.

2.2. Solute diffusion

As solidification proceeds, the growing dendrites absorb solute from neighbouring liquid. The growth process is mainly controlled by solute redistribution during solidification, which can be described according to the following equation:

$$\frac{\partial C_i}{\partial t} = \nabla\cdot\left(D_i\nabla C_i\right) + C_i\left(1 - k_0\right)\frac{\partial f_S}{\partial t} \tag{3}$$

where C and D are the solute concentration and solute diffusion coefficient, respectively, subscript i means liquid or solid, and k_0 is the solute partition coefficient. The second term on the right-hand side is included only at the S/L interface and denotes the amount of solute absorbed at the interface. More details about the solute field control equations and calculation process can be found in Reference [8].

2.3. Interface growth kinetics

The local interface equilibrium composition and solute conservation can be calculated by the following equations:

$$C_L^* = C_0 + \left[T^* - T_L + \Delta T_R\right]/m_L \tag{4}$$

$$C_S^* = k_0 C_L^* \tag{5}$$

where m_L is the liquidus slope of the phase diagram, T^* is the interface temperature, T_L is the equilibrium liquidus temperature at initial solute composition C_0, ΔT_R is the curvature undercooling, k_0 is the solute partition coefficient, and C_L^* and C_S^* are the equilibrium liquid and solid compositions, respectively.

For three-dimensional dendrite growth, the curvature undercooling ΔS_R, can be related to the weighted mean curvature, which is expressed as the following [11]:

$$\Delta T_R = \frac{1}{\Delta S_F}\sum_{i=1}^{2}\left(\gamma\left(\mathbf{n}\right) + \frac{\partial^2\gamma\left(\mathbf{n}\right)}{\partial\theta_i^2}\right)\cdot\kappa_i \tag{6}$$

where ΔS_F is the entropy of melting, κ is the curvature of the S/L interface, θ_1 and θ_2 are the two standard spherical angles of the interface normal, $\mathbf{n}$, and $\gamma(\mathbf{n})$ is the anisotropic surface energy function. In order to simplify this expression and allow numerical computation, it is assumed that these two principal curvatures are equal [18]. The curvature undercooling can be approximately given by:

$$\Delta T_R = \frac{\kappa}{\Delta S_F}\sum_{i=1}^{2}\left(\gamma\left(\mathbf{n}\right) + \frac{\partial^2\gamma\left(\mathbf{n}\right)}{\partial\theta_i^2}\right) \tag{7}$$

The function describing the dependence of the surface energy on the normal direction, $\mathbf{n}$, in the case of cubic symmetry is given by [19]:

$$\begin{aligned}\gamma\left(\mathbf{n}\right) &= \gamma_0\left(1 - 3\varepsilon\right)\left[1 + \frac{4\varepsilon}{1 - 3\varepsilon}\left(n_x^4 + n_y^4 + n_z^4\right)\right] = \\ &= \gamma_0\left(1 - 3\varepsilon\right)\left[1 + \frac{4\varepsilon}{1 - 3\varepsilon}\begin{pmatrix}\cos^4\theta_1 + \sin^4\theta_1\times \\ \times\left(1 - 2\sin^2\theta_2\cos^2\theta_2\right)\end{pmatrix}\right]\end{aligned} \tag{8}$$

$$\Gamma = \frac{\gamma_0}{\Delta S_F} \tag{9}$$

$$\theta_1 = \arccos\left(\frac{\partial f_S}{\partial x}\Big/\sqrt{\left(\frac{\partial f_S}{\partial x}\right)^2 + \left(\frac{\partial f_S}{\partial y}\right)^2}\right) \tag{10}$$

$$\theta_2 = \arccos\left(\frac{\partial f_S}{\partial z}\Big/\sqrt{\left(\frac{\partial f_S}{\partial x}\right)^2 + \left(\frac{\partial f_S}{\partial y}\right)^2 + \left(\frac{\partial f_S}{\partial z}\right)^2}\right) \tag{11}$$

where γ_0 is the isotropic interfacial energy, ε is the anisotropy coefficient, and Γ is the Gibbs-Thomson coefficient. The calculation of ΔT_R for two dimensions has been analysed in detail by Chen et al. [10].

The curvature for an interface cell with solid fraction f_S ($0 < f_S < 1$) is calculated by the following expression [20]:

$$\kappa = \frac{1}{\Delta x}\left[1 - 2\left(f_S + \sum_{i=1}^{N} f_S^i\right)/(N+1)\right] \tag{12}$$

where f_S^i is the solid fraction of the neighbouring cells, Δx is the cell size, and N is the total number of first-layer neighbouring cells, which is equal to 8 in two dimensions and 26 in three dimensions.

The increment of solid fraction for the interface cells at each time step, Δf_S, is obtained by:

$$\Delta f_S = \left(C_L^* - C_L\right)/\left(C_L^*\left(1 - k_0\right)\right) \tag{13}$$

where C_L is calculated from Eq. (3) and C_L^* is obtained based on Eq. (4). When f_S equals 1, the interface cell becomes a solid state, and its four neighbouring liquid become interface cells.

Fig. 1. Photo of casting experiment

3. Results and discussion

3.1 Solidification microstructure

The material used in this study was a U-5.5Nb alloy (by mass percent). The depleted uranium and high-purity niobium were vacuum-induction melted into an ingot in a cylindrical graphite crucible with a protective coating. In order to improve the composition homogeneity, the U-5.5Nb alloy ingot was re-melted at 1520°C for 30 min under vacuum and then cooled in the furnace. A thermocouple was positioned at the centre of the re-melt ingot (100 mm in diameter and 200 mm in height) to measure the temperature variation during the solidification process. Fig. 1 shows the photo of casting experiment. In order to investigate the as-cast microstructure of U-5.5Nb alloy, metallographic specimens were cut from the centre of the re-melted ingot. Metallographic investigation was carried out by optical microscopy (OM), and the chemical composition of examined microstructure was determined by using scanning electron microscopy (SEM) coupled with energy dispersive spectroscopy (EDS). The samples were cold mounted, mechanically polished, and electro-polished using 5% H_3PO_4 solution at 2-3 V for 2-3 s. Electro-etching in 10% oxalic acid solution at 4-5 V for 3-5 s was used for final metallographic observation.

The microstructure of the specimen after etching observed by OM and SEM is shown in Fig. 2, where the solidification microstructure displays an equiaxed dendritic structure. As can be seen in Fig. 2(a), the resistance to etching indicates that these

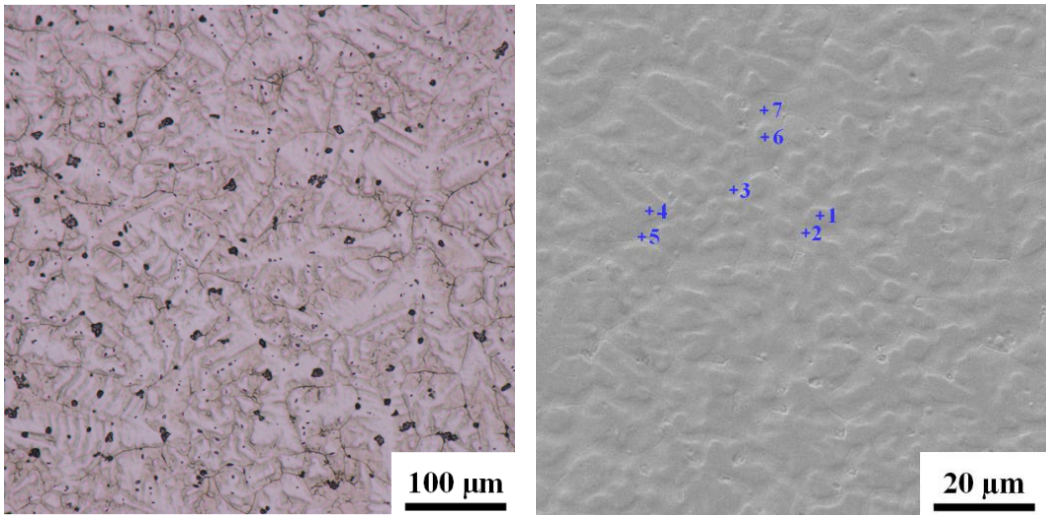

(a) (b)

Fig. 2. The microstructure of the specimen after etching observed by OM (a) and SEM (b)

first-formed regions are Nb-enriched, and the brighter area of the grain is the primary γ-phase, which is the first to solidify. The solute concentration distribution in dendritic trunks and inter-dendritic regions was analysed by the EDS point measurement. As shown in Fig. 2(b), 7 points are selected for EDS analysis, and the measured results are shown in TABLE 1. The results shows that the concentration of Nb in dendritic trunks and inter-dendritic regions are approximately 5.93-6.32 wt.% and 2.81-3.46 wt.%, respectively. From the U-Nb phase diagram [21], it can be found that the Nb concentration in the dendrite center should be equal to 11.0 wt.% (the partition ratio is assumed: $k_0 = 2$). The reason why Nb concentration (in the middle of the primary phase) diminish from 11.0 wt.% to 5.9-6.3 wt.% is probably due to the back diffusion in the solid. According to research by Wołczyński et al. [22-27], solute redistribution is the result of both solute partitioning and the back diffusion. Moreover, the solute redistribution should be measured on the central section of the dendrite [22]. However, it is very difficult to cut the selected dendrite centrally, and it maybe cause the difference of chemical composition. Nb distribution in different location of equiaxed dendrite will be explored in the future experiment. As can be seen in Fig. 2, there are inclusions (black spots) distributed at the γ grain boundary. Fig. 3 shows the morphology and composition of the inclusions of the specimen after polishing. The results show that the carbides are mostly uranium carbide.

TABLE 1

The concentration of Nb in dendritic trunks and inter-dendritic regions

Measuring positions	Nb (wt. %)
Point 1	6.32
Point 2	3.46
Point 3	3.09
Point 4	5.93
Point 5	2.92
Point 6	5.94
Point 7	2.81

3.2. Numerical simulation

The CA model was used to predict the 2-D primary dendrite growth of the U-5.5Nb alloy. The physical properties used for the simulation are listed in TABLE 2. The computational domain was divided into a 600×600 square mesh with a mesh size of Δx = 1 μm. The cooling rate used in the solidification simulation was obtained from the experimental cooling curve, and the average cooling rate was approximately 10 K/s. In the present simulation, the temperature and concentration of the liquid were assumed as uniform throughout the computational domain, and non-flux boundary conditions were incorporated in the computational domain. As the solidification proceeds, the growing equiaxed dendrites absorb solute from its neighboring liquid units. Considering the fact that the mutual diffusion coefficients between the elements is much smaller compared with the self-diffusion coefficients [28], hence, the mutual diffusion process

TABLE 2

Properties of the U-5.5Nb (wt. %) binary alloy used in simulations

Definition and symbol	Value
Liquidus temperature T_L (K)	1633
Liquidus slope m_L (K·wt.%$^{-1}$)	37.3
Liquid diffusion coefficient D_L (m^2·s^{-1})	1.05×10^{-9}
Solid diffusion coefficient D_S (m^2·s^{-1})	3.14×10^{-10}
Partition coefficient k_0	2.0
Gibbs-Thomson coefficient Γ (K·m)	1.9×10^{-7}

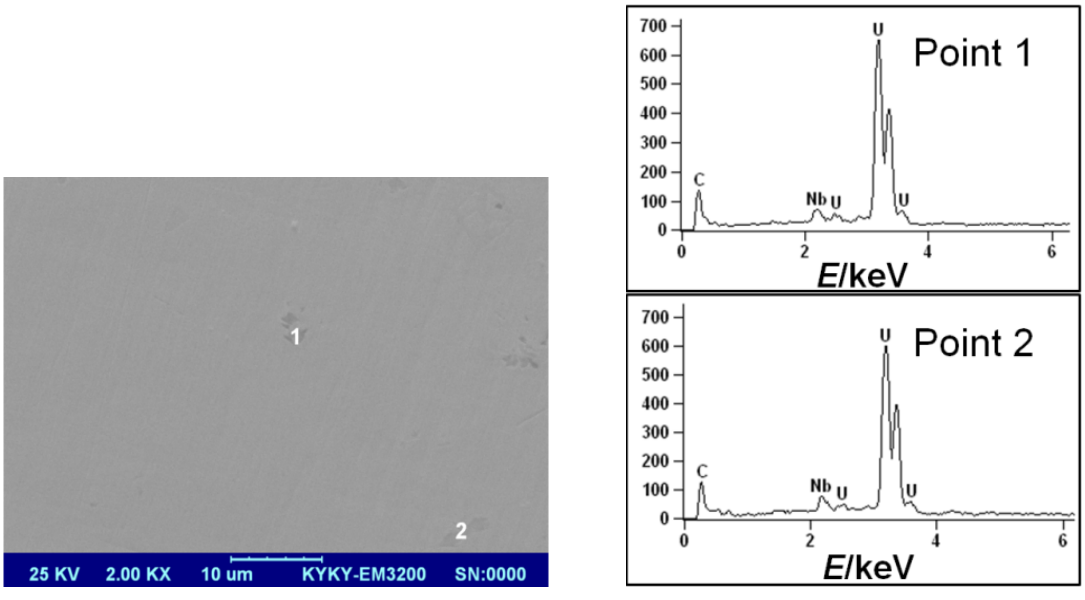

Fig. 3. SEM morphology of inclusions (a) and EDS results (b) of points 1 and 2

was neglected in the present model. Then the solute diffusion within the entire domain was calculated based on Eq. (3). In addition, for the non-equilibrium solidification, micro-segregation with complete or finite back-diffusion model may be an effective method, which was proposed by Wołczyński [24], and the coupled model allowed to calculate the solute redistribution and the amount of eutectic precipitate.

Fig. 4(a,c,e) shows the evolution of simulated equiaxed dendrite morphologies during solidification, where the green area represents liquid. The other colour areas represent the γ-phase, where different colours represent γ grains with different crystallization orientations. Fig. 4(b,d,f) shows the simulated corresponding Nb concentration. The nucleation, growth, and coarsening process of the γ-phase grains occurs with decreasing

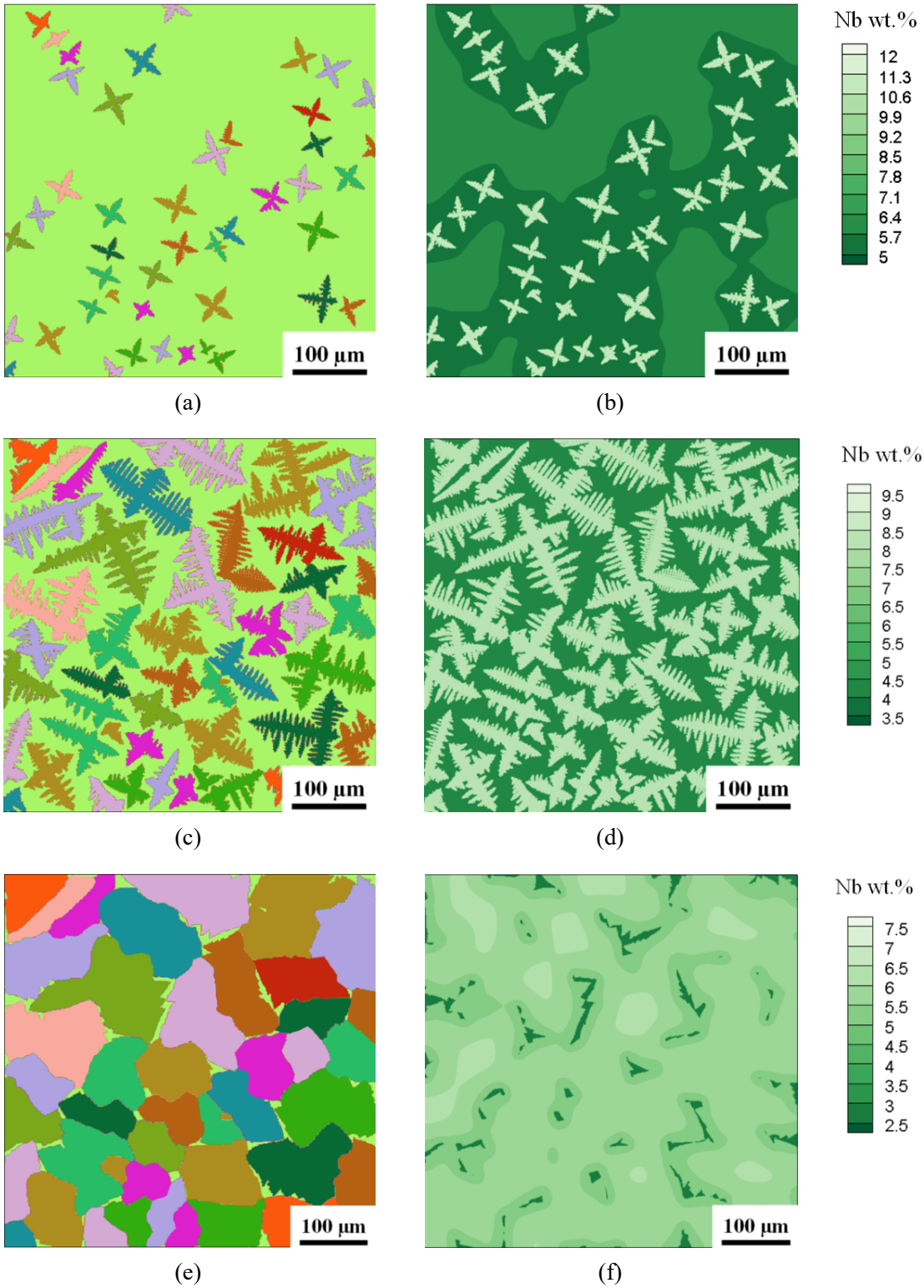

Fig. 4. Simulated dendrite microstructures (a, c, and e) and corresponding Nb concentrations (b, d, and f) of the U-5.5Nb alloy during solidification, where t = 1.9 s, 6.7 s, and 12.4 s, respectively

temperature, and the dendrites grow continuously until they meet each other. Upon successful transformation, the liquid between inter-dendritic regions and grain boundaries is separated into discrete liquid droplets in which the solute is poor, which leads to Nb micro-segregation. Fig. 5 shows the Nb concentration distribution along the centre line shown in Fig. 4(f). The regions where the Nb concentration is approximately equal to 6.21 wt.% are areas where the liquid solidified first, while the Nb concentration of the last regions to solidify is as low as 2.54 wt.%. This is probably the reason why uranium carbides are mainly distributed in the inter-dendritic regions. The simulated morphology and concentration distribution are close to the experimental results, and thus the simulated Nb concentration distribution after solidification can be used for designing and optimizing heat treatments. In addition, the experimental measurement of the solute concentration is also an effective method to investigate the micro-segregation, such as, Wołczyński [26] proposed the measurement way of the *Peclet Number* can allow to work out some maps of alloying elements segregation.

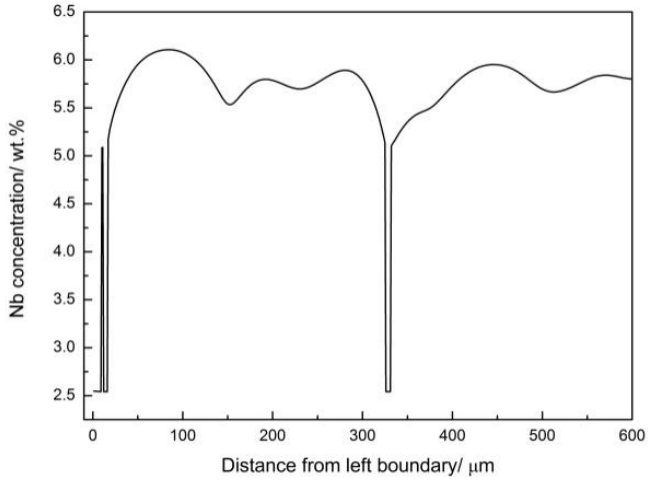

Fig. 5. Nb concentration distribution along the centre line of Fig. 4(f) at a solidifying time of 12.4 s

The CA model was also applied to simulate the 3-D equiaxed dendrite growth of the U-5.5Nb alloy. The computational domain was divided into a 200×200×200 square mesh with a mesh size of Δx =1 μm. Fig. 6 shows the evolution of the simulated 3-D dendrite morphology of the γ-phase during solidification. As shown in Fig. 6(a), nucleation occurs randomly in the calculation domain. The dendrite arms develop along the preferential growth orientations, and the dendrite morphology exhibits six-fold symmetry. Along with dendrite growth, mechanical impingement of the dendritic tips also hinders the growth of the dendrite arms (Fig. 6(b) and Fig. 6(c)). Meanwhile, competitive growth and branching phenomena can be observed in the simulated results. The results show that the model is able to simulate the growth of multi-dendrites with various crystallographic orientations and reproduce various realistic microstructural features, such as coarsening, competition of primary trunks and secondary arms, and interactions among dendrites.

4. Conclusions

In this study, a modified CA model was developed to simulate the formation and evolution of the primary phase in the U-5.5Nb alloy during the solidification process. By using the model, the 2-D and 3-D equiaxed dendrite growth of the U-5.5Nb alloy during solidification and the formation mechanism of Nb micro-segregation were investigated.

Upon successful transformation, the liquid between inter-dendritic regions and grain boundaries is separated into discrete liquid droplets in which the solute is poor, which leads to Nb micro-segregation. The regions where the Nb concentration was approximately equal to 6.21 wt.% were areas of liquid which solidified first, while the Nb concentrations of the regions which solidified last were as low as 2.54 wt.%.

To validate the model, a U-5.5Nb ingot was produced, and metallographic examination was carried out. The SEM/EDS

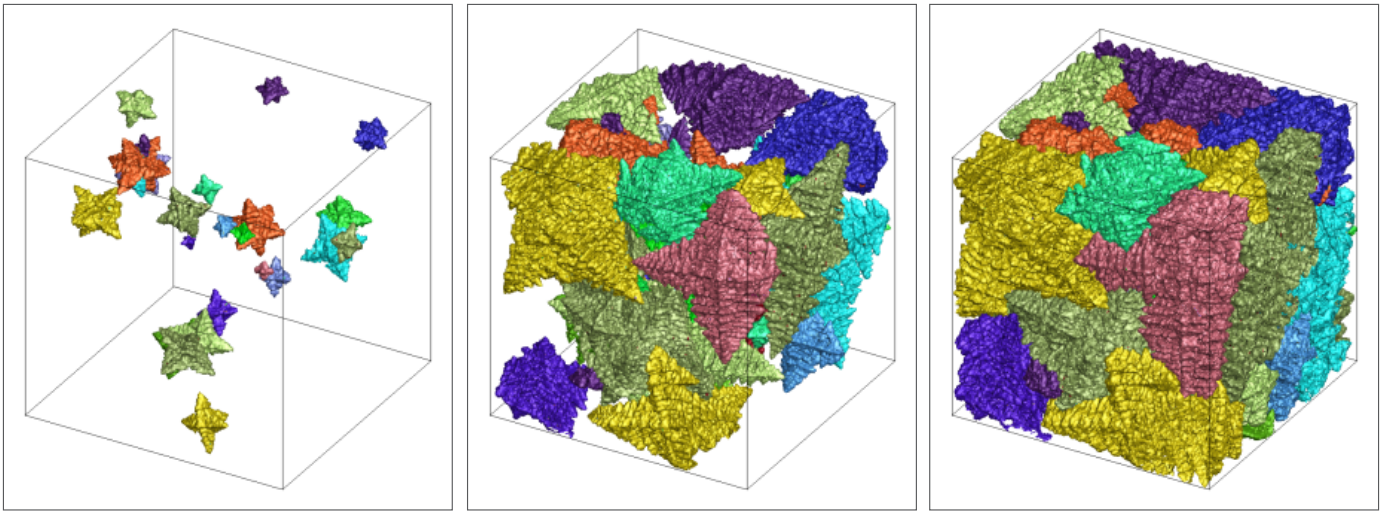

Fig. 6. Simulated evolution of 3-D multi-equiaxed dendrites in U-5.5Nb alloy during solidification: (a) t = 1.9 s; (b) t = 6.7 s; and (c) t = 12.4 s

analysis show that the concentrations of Nb in dendritic trunks and inter-dendritic regions were approximately 5.93-6.32 and 2.81-3.46 wt.%, respectively. The results show that the simulated morphology and concentration distribution are close to the experimental results.

The overall study results show that the CA model is able to simulate the growth of multi-dendrites with various crystallographic orientations and to reproduce various realistic microstructural features, such as coarsening, competition of primary trunks and secondary arms, and interactions among dendrites.

Acknowledgements

This work was supported by the Major Project of China Academy of Engineering Physics under grant No.TA1401, the Science Challenge Program of China under Grant No. TZ20160040201, the National Natural Science Foundation of China under Grant No. 51904276, and the Program for Science and Technology Innovation Talents in Universities of Henan Province under Grant No. 22HASTIT031.

REFERENCES

[1] H.M. Volz, R.E. Hackenberg, A.M. Kelly, W.L. Hults, A.C. Lawson, R.D. Field, D.F. Teter, D.J. Thoma, J. Alloy Compd. **444-445**, 217-225 (2007).
[2] X.J. Liu, Z.S. Li, J. Wang, C.P. Wang, J. Nucl. Mater. **380** (1-3), 99-104 (2008).
[3] A.M. Kelly, R.D. Field, D.J. Thoma, J. Nucl. Mater. **429** (s1-3), 118-127 (2012).
[4] R.J. Jackson, C.V. Kangas, RFP-1582 (1970).
[5] M. Rappaz, C.A. Gandin, Acta Metall. Mater. **41** (2), 346-360 (1993).
[6] W. Wang, P.D. Lee, M. McLean, Acta Mater. **51** (10), 2971-2987 (2003).
[7] Q. Du, A. Jacot, Acta Mater. **53** (12), 3479-3493 (2005).
[8] M.F. Zhu, D.M. Stefanescu, Acta Mater. **55** (5), 1741-1755 (2007).
[9] D. Gurgul, A. Burbelko, Arch. Metall. Mater. **55** (1), 53-60 (2010).
[10] R. Chen, Q.Y. Xu, B.C. Liu, J. Mater. Sci. Technol. **30** (12), 1311-1320 (2014).
[11] R. Chen, Q.Y. Xu, B.C. Liu, Comp. Mater. Sci. **105**, 90-100 (2015).
[12] A. Burbelko, D. Gurgul, E. Guzik, W. Kapturkiewicz, Arch. Metall. Mater. **60** (3), 2380-2384 (2015).
[13] X.Y. Song, G.Q. Liu, N.J. Gu, Scripta Mater. **43** (4), 355-359 (2000).
[14] A. Karma, W.J. Rappel, Phys. Rev. Lett. **77** (19), 1741-1755 (1996).
[15] I. Steinbach, C. Beckermann, B. Kauerauf, Q. Li, J. Guo, Acta Mater. **47** (3), 971-982 (1999).
[16] Z.X. Tu, J.X. Zhou, Y.J. Yin, X.Y. Ji, X. Shen, Arch. Metall. Mater. **64** (1), 119-123 (2019).
[17] W. Wołczyński, A.A. Ivanova, P. Kwapisiński, Procedia Manuf. **30**, 459-466 (2019).
[18] X.F. Zhang, J.Z. Zhao, H.X. Jiang, M.F. Zhu, Acta Mater. **60** (5), 2249-2257 (2012).
[19] S. Gurevich, A. Karma, M. Plapp, R. Trivedi, Phys. Rev. E. **81** (1), 011603 (2010).
[20] L. Nastac, Acta Mater. **47** (17), 4253-4262 (1999).
[21] J. Koike, M.E. Kassner, R.E. Tate, R.E. Rosen, J. Phase Equilib. **19**, 253-260 (1998).
[22] W. Wołczyński, J. Kloch, R. Ebner, W. Krajewski, Calphad. **25** (3), 391-400 (2001).
[23] W. Wołczyński, W. Krajewski, R. Ebner, J. Kloch, Calphad. **25** (3), 401-408 (2001).
[24] W. Wołczyński, Arch. Metall. Mater. **60** (3B), 2403-2407 (2015).
[25] W. Wołczyński, Arch. Metall. Mater. **60** (3), 2409-2414 (2015).
[26] W. Wołczyński, Arch. Metall. Mater. **63** (4), 1915-1922 (2018).
[27] W. Wołczyński, Arch. Metall. Mater. **65** (2), 653-666 (2020).
[28] R.J. Zhang, T. Jing, W.Q. Jie, B.C. Liu, Acta Mater. **54** (8), 2235-2239 (2006).